Title: **Imaging decision-related neural cascades in the human brain**

Authors: Jordan Muraskin[1], Truman R. Brown[2], Jennifer M. Walz[3], Bryan Conroy[4], Robin I. Goldman[5], Paul Sajda[1]

[1] Department of Biomedical Engineering, Columbia University, New York, NY, USA 10027

[2] Center for Biomedical Imaging, Medical University of South Carolina, Charleston, SC, USA, 29425

[3] Florey Institute of Neuroscience and Mental Health, Melbourne, Australia

[4] Philips Research, New York, NY,

[5] Center for Healthy Minds, University of Wisconsin-Madison, Madison, WI, USA, 53705

Corresponding Author: Paul Sajda, psajda@columbia.edu

Abstract

Perceptual decisions depend on coordinated patterns of neural activity cascading across the brain, running in time from stimulus to response and in space from primary sensory regions to the frontal lobe. Measuring this cascade and how it flows through the brain is key to developing an understanding of how our brains function. However observing, let alone understanding, this cascade, particularly in humans, is challenging. Here, we report a significant methodological advance allowing this observation in humans at unprecedented spatiotemporal resolution. We use a novel encoding model to link simultaneously measured electroencephalography (EEG) and functional magnetic resonance imaging (fMRI) signals to infer the high-resolution spatiotemporal brain dynamics taking place during rapid visual perceptual decision-making. After demonstrating the methodology replicates past results, we show that it uncovers a previously unobserved sequential reactivation of a substantial fraction of the pre-response network whose magnitude correlates with decision confidence. Our results illustrate that a temporally coordinated and spatially distributed neural cascade underlies perceptual decision-making, with our methodology illuminating complex brain dynamics that would otherwise be unobservable using conventional fMRI or EEG separately. We expect this methodology to be useful in observing brain dynamics in a wide range of other mental processes.

Introduction

The detailed spatiotemporal brain dynamics that underlie human decision-making are difficult to measure. Invasive techniques with sufficient temporal or spatial resolution, such as depth electrodes or cortical arrays used with epilepsy patients, are only feasible in rare cases and, in addition, do not capture activity from the entire brain. In comparison, non-invasive measures such as electroencephalography (EEG) and magnetoencephalography (MEG) suffer from poor spatial resolution, and blood oxygen level dependent functional MRI (BOLD fMRI) from poor temporal resolution and indirect coupling to neural activity (e.g. fMRI)[1]. In spite of this, EEG, MEG, and fMRI have been used individually to study perceptual decision-making in the human brain, although, by themselves they provide a limited view of the underlying brain dynamics [2].

Recently, methods enabling simultaneous acquisition of EEG and fMRI (EEG/fMRI) have led to varied analytic approaches aimed at integrating the electrophysiological and hemodynamic information contained in the joint measurements. Such approaches offer the potential to provide a comprehensive picture of global brain dynamics, and will likely offer new insights into how the brain makes rapid decisions [3,4]. Some of the techniques that have been proposed for combining multi-modal brain signals have separately analyzed the EEG and fMRI data and subsequently juxtaposed the results[5,6], while others attempt for a truly integrated approach in order to fully exploit the joint information contained in the data sets [7]. In general, simultaneous EEG/fMRI and the associated analysis techniques have been used to identify neuronal sources of EEG trial-to-trial variability, linking them to cognitive processes such as attention [8] and inhibition [9].

63 Many previous studies have used known EEG markers (P1, N2, N170, P300, α-
64 rhythm) or data driven approaches such as Independent Component Analysis (ICA) to
65 combine EEG with fMRI data [4,8-16]. One promising approach has been to use supervised
66 machine-learning techniques (e.g. classifiers) to find relevant projections of the EEG
67 data, where single-trial variability of the electrophysiological response along these
68 projections can be correlated in the fMRI space. Goldman, et al. [17], Walz, et al. [18] and
69 Fouragnan, et al. [19] have demonstrated this technique on visual and auditory paradigms.
70 This methodology has been shown to localize cortical regions that modulate with the task
71 while preserving the temporal progression of task-relevant neural activity.
72 Here we combine a classification methodology with an encoding model that
73 relates the trial-to-trial variability in the EEG to what is observed in the simultaneously
74 acquired fMRI. Encoding models have become an important machine learning tool for
75 analysis of neuroimaging data, specifically fMRI [20]. In most cases encoding models have
76 been used to learn brain activity that encodes or represents features of a stimulus, such as
77 visual orientation energy in an image/video [21-23], acoustic spectral power in sound/speech
78 [24], or visual imagery during sleep [25]. In the method presented here, we employ an
79 encoding model to directly relate the simultaneously collected data from the two
80 neuroimaging modalities—instead of features derived from the stimulus, they are derived
81 from EEG component trial-to-trial variability. Specifically, we learn an encoding in the
82 spatially precise fMRI data from the temporally precise trial-to-trial variability of EEG
83 activity predictive of the level of stimulus evidence. This approach leverages the fact that
84 the level of stimulus evidence, as measured via EEG, persists across the trial [26,27], and

that by discriminating this information in a time-localized way, one can temporally "tag" specific cortical areas by their trial-to-trial variability.

Using our framework for learning the BOLD signal encoding of task-relevant and temporally precise EEG component variability, we unravel the cascade of activity from the representation of sensory input to decision formation, decision action, and decision monitoring. A particularly novel finding is that after the activation of decision monitoring regions (i.e. ACC), we see a reactivation of pre-response networks, where the strength of this reactivation correlates with measures of decision confidence. This specific reactivation, as well as the entire spatio-temporal cascade, is completely unobservable using conventional fMRI-only or EEG-only methodologies.

Results

In this study, we used a visual alternative forced choice (AFC) task where subjects were shown brief presentations of pictures corrupted by noise and instructed to rapidly discriminate between object categories. On any given trial, the level of noise, or stimulus evidence, was varied randomly. The task itself, as well as similar visual decision-making tasks [28], is believed to engage an extensive set of cortical areas in a coordinated fashion, including regions that are responsible for sensory encoding, evidence accumulation, decision formation, and response and decision monitoring. However, the dynamic interplay of these regions has never been observed in humans. Here we exploit previously reported findings regarding the sensitivity of the EEG and fMRI signals to the level of stimulus evidence during a perceptual decision-making task. Specifically, previous work has shown differential neural responses to high vs. low

108 stimulus evidence in trial averaged EEG event-related potentials (ERPs), where this
109 difference persists across the trial[26,27]. Similarly, fMRI studies have shown that for
110 perceptual decision making tasks a number of spatially-distributed cortical areas
111 significantly correlate with the level of stimulus evidence[29,30]. We leverage the fact that
112 the level of stimulus evidence is expressed temporally in the EEG and spatially in the
113 fMRI to "tag" voxels with a time. Specifically, using a classification methodology (i.e.
114 discriminative components) we identify temporally precise expressions of the level of
115 stimulus evidence that then can be spatially localized through an encoding model of the
116 fMRI BOLD data.

117 We collected simultaneous EEG/fMRI data from 21 subjects as they performed a
118 3-AFC task discriminating between faces, cars, and houses (Fig. 1A). Subjects were
119 instructed to discriminate the object class after briefly viewing an image corrupted by
120 varying levels of noise (Fig. 1B) and respond by pressing one of three buttons. Overall,
121 subjects responded with accuracies of 94 ± 5% and 58 ± 12% and with response times of
122 634 ± 82ms and 770 ± 99ms for high and low stimulus evidence trials, respectively (Fig.
123 1 C, D). Subject accuracies and response times across stimulus types (faces, cars, houses)
124 for low stimulus evidence trials were similar; however, for high stimulus-evidence trials
125 subject accuracies were higher and response times were shorter for faces than for cars or
126 houses (See Supplemental Information Fig. S1).

127

128 *GLM based analysis of BOLD fMRI shows superposition of cortical areas correlated*
129 *with stimulus evidence*

130 A traditional general linear model (GLM) analysis of the fMRI (see Methods)
131 revealed differences in BOLD activation between the two stimulus evidence conditions
132 (Fig. 1F, SI Table 1). Brain regions showing greater BOLD activation to high vs. low
133 stimulus evidence trials included areas associated with early visual perception and the
134 default mode network[26], such as fusiform gyrus, parahippocampal gyrus, lateral occipital
135 cortex, superior frontal gyrus, and posterior cingulate cortex. Regions with greater BOLD
136 activation to low vs. high stimulus evidence trials included areas in the executive control
137 and difficulty networks, such as dorsal lateral prefrontal cortex, anterior cingulate cortex,
138 intraparietal sulcus, and insula. Overall, these GLM results for the BOLD data
139 reproduced previous results in the literature where similar stimuli and paradigms were
140 used [29](Fig. S2A).
141
142 *Extracting temporally localized EEG signatures of stimulus evidence variability*
143 The traditional fMRI results showed multiple brain regions correlated with the
144 difficulty, or stimulus evidence, of the trial; however, this traditional approach does not
145 enable one to infer the relative timing of these fMRI activations. To infer timing at a
146 scale of tens of milliseconds, we used linear classification[31,32] of the EEG to extract trial-
147 to-trial variability related to stimulus evidence at specified post-stimulus time points.
148 The basic idea is illustrated in Figure 2, where hypothetical neural activity is
149 shown for two different regions that are constituents of the perceptual decision-making
150 network. Averaging over trials would clearly reveal a difference in the mean neural
151 activity between high and low stimulus evidence. However, the two regions contribute
152 differentially to the network, with one region encoding the stimulus evidence (Region 1)

153 and the other integrating it over time (Region 2); both are sensitive to the level of
154 stimulus evidence, though varyingly so at different times in the trial. By taking
155 advantage of this sensitivity to the stimulus evidence, we can learn EEG discriminant
156 components, i.e. spatial filters, that best classify trials at different time windows given the
157 neural data. We used the trial-to-trial variability along these component directions as
158 features to uniquely tag fMRI voxels with the specific time window of the component.
159 This tagging is done by building an encoding model of the features, given the BOLD
160 signal, details of which are described in the following section.

161 We constructed EEG components by learning linear classifiers at 25ms steps,
162 starting from stimulus onset to 50ms past the average low stimulus evidence response
163 time. We chose a time step of 25ms due to an empirical analysis showing a half width of
164 50ms in the temporal autocorrelation of the EEG data, though in principle this
165 methodology allows for temporal resolution up to the EEG sampling rate. Each classifier
166 was associated with a set of discriminant values, which can be represented as a vector y_τ;
167 each element of the vector is the distance of a given trial to the discrimination boundary
168 for the classifier at time step τ (Fig. 2). This distance can be interpreted as a measure of
169 the EEG classifier's estimate of the level of stimulus evidence for that trial[17,18,31-34].

170 Results of the EEG analysis show discriminating information for stimulus
171 evidence spanning the trial (see Fig. 4A), beginning roughly 175ms post-stimulus to past
172 the average response times. A dip occurs around 300ms, indicating stimulus evidence is
173 less discriminative at this time and serves to demarcate early and late cognitive processes.
174 The early process corresponded to the time of the D220 ERP component, which has been
175 shown to modulate with the degree of task difficulty, whether via stimulus noise or task

demands[35]. The later and more prolonged component is likely related to more complex cognitive and motor preparatory processes that differ between high and low stimulus evidence trials. Importantly, although the early and late EEG components were both discriminative, we found their trial-to-trial variability to be uncorrelated (Figs. 4B and S3E), indicating that while the discriminating information (level of stimulus evidence) persists across the trial, it couples differently to processes across time.

An encoding model links fMRI activations with temporally distinct EEG trial-to-trial variability

After extracting the trial-to-trial variability from the EEG discriminant components, feature vectors y_τ are collected across time steps, τ, along with a response time vector to construct a matrix *Y*. This matrix is the temporally precise representation of the trial-to-trial EEG variability that reflects high vs. low stimulus evidence. An encoding model is then fit, namely a model in which weights are estimated for each time-localized EEG window, to predict the trial-to-trial variability of the BOLD response for each fMRI voxel. Figure 3 shows a schematic of the encoding model framework we used and compares it to a traditional encoding model constructed by using features derived directly from the stimulus. Rather than constructing a map that directly relates each voxel to a type of stimulus feature, such as whether it encodes edges, motion or some semantic concept such as "animal" [21-23,36-38], our model is used to construct maps that label voxels by the time window of the variability they encode – i.e. it "tags" each voxel with a "time", or set of times, when it encodes the variability in the given EEG discriminant component(s).

199 It is important to note that this approach does not attempt to improve source
200 localization typically done for EEG/MEG studies. Our approach instead provides the
201 temporal resolution of EEG (ms) and the spatial resolution of fMRI (mm) without the
202 need to solve the ill-posed inverse solution and make the many associated assumptions
203 required for reliable source-localization results[39].
204 An example of the quality of the encoding model is shown in Fig. 4C (see also
205 Fig. S2B) where significant voxels from the encoding model are shown in yellow. Fig.
206 4D shows the trial-to-trial variability of BOLD signal at a specific voxel, comparing it to
207 the variability predicted by the encoding model. Additional validity of the encoding
208 model and single subject results are presented in the Supplemental Information (Fig.
209 S4A/B). The encoding model was also evaluated as a decoding model (see Methods) with
210 the BOLD activity used to predict the trial-to-trial variability in the EEG for unseen
211 data—data on which the encoding model was not trained. Fig. 4E shows these results,
212 expressed as the correlation between the measured and predicted EEG trial-to-trial
213 variability across the 800ms epoch. The shape of the curve is highly consistent with that
214 observed for the EEG data itself (comparing Fig. 4A and Fig. 4E) (additional analysis of
215 the fidelity of the model is provided in the SI, Fig. S3).
216 Given the encoding model, we unwrap the BOLD activity across time by
217 identifying weights that are consistent across subjects in space and time (see Methods).
218 Fig. 5 shows these results for a group level analysis. We observe a progression of activity
219 (see Movie S1), at 25ms resolution, which proceeds simultaneously down the dorsal and
220 ventral streams of visual processing for the first 250ms. After that the cascade becomes
221 more complex with activation in the IPS at 425ms and 750ms (see Fig. 6A), reactivation

222 of the SPL at 675ms and activation of ACC at 600ms along with other regions found in
223 the traditional fMRI results. (see Fig. S5, Tables S2 and an additional analysis using
224 dynamic causal modeling [40]). The reactivation pattern is particularly significant since it
225 would not be observable via a traditional fMRI general linear model (GLM) analysis,
226 which integrates over time and thus superimposes these activities. For example, the
227 changing sign of the middle temporal gyrus (MT) encoding weights in Fig. 6A
228 manifested as no activity in the MT for the traditional fMRI GLM analysis—the change
229 in sign canceled the effective correlation in the GLM (see Fig. 1F and Fig. S1). The areas
230 of activation we find are consistent with previous reports in the literature for human
231 subjects[29,30]; however, here we are able to link activations across time in a way that was
232 previously only possible with invasive techniques.
233
234 *Cortical reactivation correlates with decision confidence*
235 Further analysis of the spatiotemporal dynamics (see Fig. 6B), shows that the
236 reactivation pattern in the network occurs after decision-monitoring areas become
237 engaged (i.e. after ACC). Spontaneous reactivation, or "replay", of neural activity in the
238 human brain has been observed and believed to be important for memory consolidation[41]
239 and more recently has been hypothesized to play a role in perceptual decision-making by
240 enabling the formation of decision confidence[42]. To test the hypothesis that the
241 reactivation activity we see is in fact related to decision confidence, we used a
242 hierarchical drift diffusion model (DDM)[43,44] to fit the behavioral data for high and low
243 stimulus evidence conditions (see Methods). Specifically, our model enables us to define
244 a proxy for decision confidence based on the DDM fits to the behavior[45,46]. Correlating

245 the reactivation level to this confidence proxy shows a strong and significant monotonic
246 relationship between confidence and the level of reactivation (high stimulus evidence-
247 slope=0.037±0.008, t=4.657, $p=3.2x10^{-6}$; low stimulus evidence-slope=0.062±0.008,
248 t=7.754, $p=8.88x10^{-15}$), with low stimulus evidence trials reactivated more strongly than
249 high stimulus evidence trials (difference in slopes=-0.025±0.011, t=2.189, p=0.029)(see
250 Fig. 7 and Fig. S7). Additionally, reactivation amplitude correlates with behavioral
251 accuracy (Fig. S8) (high stimulus evidence, slope=0.0115±0.0047, t=2.41, p=0.016; low
252 stimulus evidence, slope=0.0104±0.0047, t=2.19, p=0.028). Recursive feature elimination
253 showed that the IPS/SPL and dorsal lateral prefrontal cortex (DLPFC) clusters
254 contributed the most to reactivation/confidence proxy correlation (Fig. 7C).
255
256
257 ***Discussion***
258 We have shown that linking simultaneously acquired EEG and fMRI using a novel
259 encoding model enables imaging of high-resolution spatiotemporal dynamics that
260 underlie rapid perceptual decision-making — decisions made in less than a second. This
261 method, which resolves whole-brain activity with EEG-like temporal resolution, was
262 shown to uncover reactivation processes that would otherwise be masked by the temporal
263 averaging and slow dynamics of traditional fMRI. More broadly, our results
264 demonstrated a general non-invasive data-driven methodology for measuring high
265 spatiotemporal latent neural processes underlying human behavior.
266 This approach temporally "tags" the BOLD fMRI data by encoding the trial-to-
267 trial variability of the temporally precise task relevant components in simultaneously

acquired EEG. In effect, the EEG discrimination indexes the activity of interest at high temporal resolution, defining a feature space, and the trial-to-trial variability of these discriminant components becomes the specific feature values used in the encoding model. For the case presented here, this variability was used to tease apart the cascade of activity modulated by stimulus evidence across the trial, and this allowed us to observe, as never seen before, the spatiotemporal brain dynamics underlying a perceptual decision.

Previous studies have sought to generalize the timing diagram of a perceptual decision through multi-unit recordings in non-human primates[47,48] or more broadly in humans[29,30] using fMRI. Our results confirmed the general temporal ordering of activations found previously (early visual processing, decision formation, decision monitoring). However, there was a possibility the temporal order we observed using our technique was an artifact of our methodology. To assess this possibility, we performed additional analyses using dynamic causal modeling (DCM) to further validate the temporal activation sequence (see Fig. S6) and show, using a different set of assumptions and method, that the temporal sequence we observe is highly likely under a set of alternative sequences. We found that the most likely model is the one consistent with the time course inferred from our encoding model. The DCM results provide additional evidence that the temporal profile uncovered by the encoding model is a likely temporal decomposition of the superimposed fMRI activations.

The approach we present requires that EEG and BOLD data be collected simultaneously and not in separate sessions in order to exploit the correlations in trial-to-trial variability to “tag” the BOLD data. To show the importance of collecting the data simultaneously, we ran a control analysis that randomly permuted the trials within their

291 stimulus evidence class, thus effectively simulating an EEG and BOLD dataset collected
292 separately. By destroying the link between the EEG and BOLD trials, the encoding
293 model failed to find any consistent activation (Fig. S11/12), indicating the necessity of
294 simultaneous acquisition.

295 Alternative techniques for fusing simultaneous EEG-fMRI typically do not
296 exploit EEG across the trial and instead only analyze specific ERP components or time
297 windows of interest [4,8,10,12-19,49,50]. Results from these techniques identify regions that
298 modulate with the specific components, but yield limited information about the timing of
299 other task-relevant regions seen in traditional fMRI contrasts. The methodology
300 developed here extends the work of Goldman, et al. [17] and Walz, et al. [18] by combining
301 their EEG data reduction techniques with techniques developed for encoding stimulus
302 features onto BOLD data[20-23,36,38], ultimately providing a framework for labeling voxels
303 in task-relevant fMRI contrasts with their timing information (Fig. S2C/E/F).

304 Clearly, other EEG components that are task-related can be isolated and could
305 potentially be used to "tag" BOLD data. The sliding window linear classification used
306 here acts to reduce the EEG data along a dimension that categorizes stimulus evidence;
307 however, this could be replaced by any other data reduction technique, such as
308 temporally windowed ICA or PCA. Variability along these component directions could
309 then be used in the encoding model to link with the simultaneously collected BOLD data.
310 The choice of data reduction technique (i.e. feature space) would be highly dependent on
311 the nature of the inferences.

312 Our methodology enabled us to observe reactivation of the pre-response network,
313 spatiotemporal dynamics that would be masked using traditional fMRI analysis.

Interestingly, the reactivation terminated in a network that included the MFG, SPL, and IPS, similar areas previously reported to be reactivated in metacognitive judgments of confidence in perceptual decisions[42,51,52]. In addition, these areas contributed the most to the correlation to confidence proxy (Fig. 7C). Gherman and Philiastides [53] observed this network using a multivariate single-trial EEG approach, coupled with a distributed source reconstruction technique. Fleming, et al. [42] and Heereman, et al. [54] used BOLD fMRI to show that areas in this network negatively correlate with subjective certainty ratings. Unique to our findings, we saw this reactivation on a single-trial basis after engagement of the ACC, which has been shown to be involved in decision monitoring[53,55], and also observed the dynamic sequence leading up to this network reactivation. Our results showed that reactivation/replay occurred on a trial-to-trial basis after a decision, was stronger for difficult decisions, and correlated with decision confidence.

A potential confound in our analysis is that the timing of the reactivation overlaps with some of the response times. To check if the reactivation was pre or post response, we implemented a response-locked encoding model analysis (Fig. S9). The response-locked results showed significant activation pre-response that overlaps with the reactivation network from the stimulus locked analysis. In addition, trial-to-trial reactivation taken from pre-response clusters correlates with confidence proxy similarly to the stimulus locked results (Fig. S10). This provides further evidence that the reactivation is occurring pre-response.

The encoding model we developed was able to decompose traditional fMRI activation maps into their temporal order with significant voxel overlap between the encoding model results and traditional results. The encoding model was also able to show

regions that were activated at multiple time points throughout the decision, indicating temporal dynamics that were hidden previously. The regions of activation we found are consistent with earlier findings; however, the work here provided the precise temporal decomposition of these previously reported, temporally superimposed regions of activation. In general, we have shown that simultaneously acquired EEG/fMRI data enables a novel non-invasive approach to visualize high resolution spatial and temporal processing in the human brain with the potential for providing a more comprehensive understanding of the neural basis of complex behaviors.

Methods

Subjects

21 subjects (12 male, 9 female; age range 20-35 years) participated in the study. The Columbia University Institutional Review Board (IRB) approved all experiments and informed consent was obtained before the start of each experiment. All subjects had normal or corrected-to-normal vision.

Stimuli

We used a set of 30 face (from the Max Planck Institute face database), 30 car, and 30 house (obtained from the web) gray scale images (image size 512x512 pixels, 8 bits/pixel). They were all equated for spatial frequency, luminance, and contrast. The stimulus evidence (high or low) of the task was modulated by systematically modifying the salience of the image via randomization of image phase (35% (low) and 50% (high) coherence)[56].

Experimental task

360 The stimuli were used in an event-related three-alternative forced choice (3-AFC) visual
361 discrimination task. On each trial, an image -- either a face, car, or house -- was presented
362 and subjects were instructed to respond with the category of the image by pressing one of
363 three buttons on an MR compatible button controller. Stimuli were presented to subjects
364 using E-Prime software (Psychology Software Tools) and a VisuaStim Digital System
365 (Resonance Technology) with 600x800 goggle display. Over four runs, a total of 720
366 trials were acquired (240 of each category with 120 high coherence trials) with a random
367 inter-trial interval (ITI) sampled uniformly between 2-2.5s. Each run lasted for 560
368 seconds.

369 *fMRI acquisition*

370 Blood-oxygenation-level-dependent (BOLD) T2*-weighted functional images were
371 acquired on a 3T Philips Achieva scanner using a gradient-echo echo-planar imaging
372 (EPI) pulse sequence with the following parameters: Repetition time (TR) 2000ms, echo
373 time (TE) 25ms, flip angle 90°, slice thickness 3mm, interslice gap 1mm, in-plane
374 resolution 3x3mm, 27 slices per volume, 280 volumes. For all of the participants, we also
375 acquired a standard T1-weighted structural MRI scan (SPGR, resolution 1x1x1mm).

376 *EEG acquisition*

377 We simultaneously and continuously recorded EEG using a custom-built MR-compatible
378 EEG system[57,58], with differential amplifiers and bipolar EEG montage. The caps were
379 configured with 36 Ag/AgCl electrodes including left and right mastoids, arranged as 43
380 bipolar pairs. Bipolar pair leads were twisted to minimize inductive pickup from the
381 magnetic gradient pulses and subject head motion in the main magnetic field. This
382 oversampling of electrodes ensured data from a complete set of electrodes even in

instances when discarding noisy channels was necessary. To enable removal of gradient artifacts in our offline preprocessing, we synchronized the EEG with the scanner clock by sending a transistor– transistor logic pulse at the start of each image volume. All electrode impedances were kept below 20 kΩ, which included 10 kΩ resistors built into each electrode for subject safety.

Functional image pre-processing.

Image preprocessing was performed with FSL (www.fmrib.ox.ac.uk/fsl/). Functional images were spatially realigned to the middle image in the times series (motion-correction), corrected for slice time acquisition, spatially smoothed with a 6mm FWHM Gaussian kernel, and high pass filtered (100s). The structural images were segmented (into grey matter, white matter and cerebro-spinal fluid), bias corrected and spatially normalized to the MNI template using 'FAST' [59]. Functional images were registered into MNI space using boundary based registration (BBR)[60].

EEG data preprocessing.

We performed standard EEG preprocessing offline using MATLAB (MathWorks) with the following digital Butterworth filters: 0.5 Hz high pass to remove direct current drift, 60 and 120 Hz notches to remove electrical line noise and its first harmonic, and 100 Hz low pass to remove high-frequency artifacts not associated with neurophysiological processes. These filters were applied together in the form of a zero-phase finite impulse response filter to avoid distortions caused by phase delays. We extracted stimulus-locked 1500 ms epochs (-500:1000) and subtracted the mean baseline – -200 ms to stimulus onset – from the rest of the epoch. Through visual inspection, we discarded trials

406 containing motion and/or blink artifacts, evidenced by sudden high-amplitude
407 deflections.

408 *Sliding window logistic regression.*

409 We used linear discrimination to associate each trial with the level of stimulus evidence
410 represented in the EEG. We considered high stimulus and low stimulus evidence trials
411 irrespective of behavioral accuracy. Regularized logistic regression was used as a
412 classifier to find an optimal projection for discriminating between high and low stimulus
413 evidence trials over a specific temporal window. A sweep of the regularization
414 parameters was implemented using FaSTGLZ[61]. This approach has been previously
415 applied to identify neural components underlying rapid perceptual decision-making
416 [17,18,31,33,34,45,50,62].

417 Specifically, we defined 50ms duration training windows centered at time, τ,
418 ranging from stimulus onset to 800ms following the stimulus in 25ms steps. We used
419 logistic regression to estimate a spatial weighting, on N EEG channels, vector (w_τ which
420 is N x 1) that maximally discriminated between EEG sensor array signals E for each class
421 (e.g., high vs. low stimulus evidence trials):

422 $$y_\tau = w_\tau^T E_\tau \quad (1)$$

423 In eqn. 1, E_τ is an N x p vector (N sensors per time window τ by p trials). For our
424 experiments, the center of the window (τ) was varied across the trial in 25ms time-steps.
425 We quantified the performance of the linear discriminator by the area under the receiver
426 operator characteristic (ROC) curve, referred to here as AUC, using a leave-one-out
427 procedure. We used the ROC AUC metric to characterize the discrimination performance
428 as a function of sliding our training window (i.e., varying τ). For each subject, this

429 produced a matrix Y where the rows corresponded to trials and the columns to training
430 windows, i.e. Y is the combination of the calculated y_τ for each time window.
431 *Traditional fMRI analysis.*
432 We first ran a traditional general linear model (GLM) fMRI analysis in FSL, using
433 event-related (high and low stimulus evidence) and response time (RT) variability
434 regressors. The event-related regressors comprised boxcar functions with unit amplitude
435 and onset and offset matching that of the stimuli. RT variability was modeled using the z-
436 scored RT as the amplitude of the boxcars with onset and offset matching that of the
437 stimulus, and these were orthogonalized to the event-related regressors.
438 Orthogonalization was implemented using the Gram-Schmidt procedure[63] to decorrelate
439 the RT regressor from all other event-related regressors. All regressors were convolved
440 with the canonical hemodynamic response function (HRF), and temporal derivatives
441 were included as confounds of no interest. An event-related high versus low stimulus
442 evidence contrast was also constructed. A fixed-effects model was used to model
443 activations across runs, and a mixed-effects approach was used to compute the contrasts
444 across subjects. Activated regions that passed a family-wise error (FWE) [64] corrected
445 cluster threshold of $p < 0.01$ at a z-score threshold of 2.57 were considered significant.
446 *fMRI deconvolution.*
447 Associating fMRI data to each trial is challenging for two main reasons: (a) the temporal
448 dynamics of the hemodynamic response function (HRF) evolve over a longer time-scale
449 than the mean ITI of the event-related design, resulting in overlapping responses between
450 adjacent trials; and (b) the ITI was random for each trial so that the fMRI data was not
451 acquired at a common lag relative to stimulus onset. To overcome these issues, we

452 employed the `least squares - separate' (LS-S) deconvolution[65] method to estimate the
453 voxel activations for each trial. For every trial, the time series of each voxel was
454 regressed against a “signal" regressor and a “noise" regressor. The “signal" regressor was
455 the modeled HRF response due to that trial (a delta function centered at stimulus onset
456 convolved with a canonical HRF), while the “noise" regressor was the modeled HRF
457 response due to all other trials (superimposed linearly). The resulting regression
458 coefficients of the “signal" regressor represented the estimated voxel activations due to
459 that trial. These voxel activations were then organized into a single brain volume per trial.
460 We extracted 58697 voxels from a common gray matter group mask at 3 mm^3 spatial
461 resolution that excluded white matter and CSF and assembled the resulting voxel
462 activations into rows of the data matrix F.

463 *Single subject encoding model.*

464 All encoding model analyses were performed in MATLAB. To relate the EEG data with
465 the fMRI, we devised a subject-wise spatio-temporal decomposition using singular value
466 decomposition (SVD). Let F be an m x p matrix denoting m-voxels and p-trials that is the
467 deconvolved high and low stimulus evidence fMRI data for each trial. Let Y be the r x p
468 matrix denoting r-windows (33 EEG_τ windows and response time (RT)) and p-trials. For
469 each trial, the first row of Y is the response times while subsequent rows are the y values
470 at each window time. Let W be an m x r matrix that is the weights on Y that solve for F.

471 $$F = WY \quad (2)$$

472 Normally, if we solve for W using the least squares approach, we get:

473 $$W=(FY^T)(YY^T)^{-1} \quad (3)$$

However, each time point might be highly correlated with its neighbors, which reduces the stability of the least-squares regression. We can use SVD to reduce the feature space and improve our estimation of W (the weights on each window). Then for a leave-one-out cross validation, we hold out a single trial from the EEG Y matrix and the corresponding volume from the fMRI data F and train on the remaining trials. We repeated this for all trials.

$$Y^{Train}=U\Sigma V^{T} \tag{4}$$

Where U is an r x r orthonormal matrix, Σ is a r x p diagonal matrix and V is a p x p orthonormal matrix. After SVD on Y^{Train}, we reduced the feature dimensions on Y^{Train} to retain 75% of the variance by only keeping v components. To do this, we selected the first v rows of Σ and zeroed the other rows. We now have $\tilde{\Sigma}$ as our reduced spaced matrix. If we now recalculate our least squares solution where we have replaced Y by its reduced form $U\tilde{\Sigma}V^{T}$ in equation 3:

$$\hat{W} = (F^{Train}V\tilde{\Sigma}^{T})(\Sigma\Sigma^{T})^{-1}U^{T} \tag{5}$$

So for each leave one out fold, we first calculated the SVD of the training set. We then calculated the number of components to keep and then solve for $\hat{W}$, the weight estimate per fold. To test, we then applied the weights to the left-out test data Y^{Test} to estimate the encoded fMRI data $\hat{F}$ for the encoding part:

$$\hat{F} = \hat{W}Y^{Test} \tag{6}$$

While for the decoding model using the left out test data F^{Test}:

$$\hat{Y} = \hat{W}^{T}F^{Test}(\hat{W}^{T}\hat{W})^{+} \tag{7}$$

Here, $\hat{W}^{T}\hat{W}$ is not invertible, and so we used the pseudo-inverse.

At this point, we have $\hat{F}$, a m x p matrix with m voxels by p trials. For each voxel j, we calculated the correlation of $\hat{F}_j$ with F_j, resulting in the matrices R^{fMRI} (Pearson Correlation Map) and P^{fMRI} (p-value map of the Pearson Correlation) that are m x 1. The P^{fMRI} was then converted to a z-score map. We constructed the m x r weight matrix W by taking the average of all the trained $\hat{W}$ matrices. To test which time windows were significant, we also calculated, R_τ^{EEG}, the correlation between $\hat{Y}_\tau$ and Y_τ.

Group level spatio-temporal analysis.

For group level statistics, we first analyzed the R_τ^{EEG} vectors across all subjects. The R_τ^{EEG} vectors were converted into their p-values, and for each time window (τ), used to compute combined Stouffer p-values [66]. These group level results were then false discovery rate corrected (FDR) for multiple comparisons[67]. To identify group level voxels where our model predictions were significant, each subject's p-value maps for the leave-one-out correlation were converted into their respective z-values, and voxel-wise significance was calculated using threshold-free cluster enhancement (TFCE) using a non-parametric randomization procedure implemented in FSL[68]. Voxels were considered significant if they passed a conservative false discovery rate threshold of $p<0.01$.

These significant voxels were then used as a mask to temporally localize activations by computing the voxels that were consistent in their direction (positive (high stimulus evidence) or negative (low stimulus evidence)) and timing (τ window). To this end, we implemented a spatio-temporal TFCE (stTFCE) in both space (neighboring voxels) and time (neighboring time windows - response time window not included) and computed significance through a randomization procedure. 33000 permutations (1000 permutations per window) were run by randomly altering the sign of each subject and the

519 temporal ordering of the windows, as we were testing whether the weights were
520 consistent in sign, voxel space, and temporal window. P-values were calculated by
521 comparing the true stTFCE value with the distribution of permuted values. Again, voxels
522 were considered significant if they passed FDR correction at $p<0.05$ (high stimulus
523 evidence: FDR-Corrected $p<0.0019$, low stimulus evidence: FDR-Corrected $p<0.00036$).
524 Note, that now our number of multiple comparisons was the number of voxels in the
525 FDR-mask (20256) times the number of time windows (33). We analyzed the response
526 time separately with a standard TFCE randomization procedure implemented in FSL
527 (Fig. S2D).

528 *Dynamic causal modeling.*

529 To validate the encoding model timing, we implemented single-state linear
530 dynamic causal modeling (DCM) using DCM10 in SPM8 [69], and applied this to the
531 BOLD data to test the hypothesis that the temporal sequence of BOLD activations we
532 found in our EEG-fMRI encoding method was most likely, relative to other possible
533 sequences of these same activations, given only the BOLD data. We used the results of
534 the encoding model to select seven regions of interest that spanned the entire trial. For the
535 first region (labeled 175 in our figures), we computed the union of activations during the
536 175ms and 200ms windows. Activations of the 225ms (225) and 250ms combined with
537 275ms (250) windows become the second and third regions. We computed the union of
538 activations during the 325ms and 350ms windows to create the fourth (325). For the fifth
539 region (400), we computed the union of the activations during the 400ms-450ms
540 windows. For the sixth region (650), we computed the union of the activations during the
541 650ms and 675ms windows. Finally, the union of the activations during the 725-800ms

542 windows was computed to create the seventh region (725). We removed any overlapping
543 voxels between any of the regions and then extracted time series from individual
544 subjects' preprocessed functional data in MNI space by estimation of the first principal
545 component within each region.

546 We constructed 11 models (Figure S6) to investigate the directed connectivity of
547 these regions and validate the temporal ordering found by the encoding model. Each
548 model was feed-forward with first node in each model as the input region. The first
549 model was the temporal ordering of the regions inferred from our EEG-fMRI encoding
550 model analysis. For five of the models, we randomized the temporal ordering of the early
551 regions (175, 225, 250) and the late regions (325, 400, 650, 725) separately. For the other
552 five models, we fully randomized the temporal ordering of all the regions.

553 We used fixed-effects Bayesian model selection (BMS) to compare these 11
554 models both on a single-subject level and at the group level. BMS balances model fit and
555 complexity, thereby selecting the most generalizable model. It estimates the relative
556 model evidence and provides a distribution of posterior probabilities for all of the models
557 considered. We also compared families of similar models[70]; the model space was divided
558 into two families (early/late or fully randomized).

559

560 *Drift Diffusion Model (DDM) and Confidence Proxy.*

561 The DDM models decision-making in two-choice tasks. Here, we treated the decision
562 (correct vs. incorrect) as our two choices. A drift-process accumulates evidence over time
563 until it crosses one of two boundaries (upper or lower) and initiates the corresponding
564 response[68]. The speed with which the accumulation process approaches one of the two

boundaries (a) is called drift-rate (v) and represents the relative evidence for or against a particular response. Recently, Philiastides, et al. [45] showed that for conditions in which the boundary (a) does not change, a proxy for decision confidence for each trial (i) can be computed by $1/\sqrt{RT_i - T_{non}}$.

We used Hierarchical Bayesian estimation of the Drift-Diffusion Model in Python (HDDM) to calculate the drift rate (v), decision boundary (a) and non-decision time T_{non} for each subject [43]. Specifically, we modeled high and low stimulus evidence response time data separately. This was to ensure our confidence proxies were consistent within trial types. We included the response time and whether the subject got the trial correct. HDDM obtains a sequence of samples (i.e., a Markov chain Monte Carlo; MCMC) from the posterior of each parameter in the DDM. In our model, we generated 5000 samples from the posteriors, the first 1000 (burn-in) samples were discarded, and the remaining samples were thinned by 5%.

After modeling the DDM process, each trial's (i) confidence proxy (CP) for each subject (j) was computed by $CP_{i,j} = 1/\sqrt{RT_i - T_{non,j}}$ and then z-scored across trials where $T_{non,j}$ was varied for high or low stimulus evidence trials, separately. Therefore, CP was a measure of relative trial confidence within difficulty levels.

Confidence Proxy and Decision Replay.

Trial to trial reactivation amplitude was defined as $Y^R_{j,i} = W^T_{j,PostACC} F_{j,i}$ for each subject (j) and trial (i), where $W_{postACC}$ is the weight matrix from the encoding model thresholded by voxels that were significant in the group results from the 600-800ms

587 windows. The mean of the $Y_{j,i}^{R}$ across time becomes a measure of "decision replay"
588 strength for that trial (more negative y's indicate more replay activation, more positive y's
589 indicate less replay activation). $Y_{j,i}^{R}$ was quintiled for high and low stimulus evidence
590 and the average confidence proxy was calculated within each quintile (Fig. 7). A linear
591 mixed effects model[71] was used to test if the slope of confidences across quintile
592 grouping, $Y_{j,i}^{R}$, were significantly different from 0 while including stimulus evidence as a
593 condition. Separate similar analyses with non-replay windows (175-250ms) and testing
594 for behavioral accuracy were also performed (Fig. S7-8). To test the contribution of each
595 cluster to the correlation with confidence, we implemented recursive feature elimination,
596 where our features were clusters of significant voxels (> 48 voxels) during the 600-
597 800ms time window. This procedure removed clusters from the 'replay' network before
598 calculating trial-to-trial reactivation. We then calculated the percent change in slope
599 (reactivation x confidence proxy) when the cluster was removed compared to the total
600 network. This procedure ranks cluster importance by sorting which clusters, when
601 removed, had the strongest negative effect on slope height.
602

603 ***Author Contributions***

604 Conceptualization, J.M. and P.S.; Methodology, J.M., T.R.B., J.W. B.C., R.I.G. and P.S.;
605 Investigation, J.M.; Software, J.M., B.C.;Writing – Original Draft, J.M. and P.S.; Writing
606 – Review & Editing, J.M., T.R.B., R.I.G., J.W., and P.S. ; Funding Acquisition, P.S. ;
607 Resources, J.M., T.R.B., J.W. B.C., R.I.G. and P.S.; Supervision, T.R.B and P.S.
608

609 ***Acknowledgements***

We would like to thank Jianing Shi for assistance in collecting the EEG/fMRI data. This work was funded by National Institutes of Health Grant R01-MH085092, DARPA under Contract NBCHC090029 and the Army Research Laboratory and under Cooperative Agreement Number W911NF-10-2-0022.

References

1 Logothetis, N. K. What we can do and what we cannot do with fMRI. *Nature* **453**, 869-878, doi:10.1038/nature06976 (2008).

2 Alexander, D. M., Trengove, C. & van Leeuwen, C. Donders is dead: cortical traveling waves and the limits of mental chronometry in cognitive neuroscience. *Cognitive Processing*, doi:10.1007/s10339-015-0662-4 (2015).

3 Jorge, J. o., van der Zwaag, W. & Figueiredo, P. c. EEG-fMRI integration for the study of human brain function. *NeuroImage* **102**, 24--34, doi:10.1016/j.neuroimage.2013.05.114 (2014).

4 Huster, R. J., Debener, S., Eichele, T. & Herrmann, C. S. Methods for simultaneous EEG-fMRI: an introductory review. *The Journal of neuroscience : the official journal of the Society for Neuroscience* **32**, 6053-6060, doi:10.1523/jneurosci.0447-12.2012 (2012).

5 Plichta, M. M. *et al.* Simultaneous EEG and fMRI Reveals a Causally Connected Subcortical-Cortical Network during Reward Anticipation. *Journal of Neuroscience* **33**, 14526-14533, doi:10.1523/jneurosci.0631-13.2013 (2013).

6 Yuan, H. *et al.* Negative covariation between task-related responses in alpha/beta-band activity and BOLD in human sensorimotor cortex: an EEG and fMRI study of motor imagery and movements. *NeuroImage* **49**, 2596-2606, doi:10.1016/j.neuroimage.2009.10.028 (2010).

7 Dahne, S. *et al.* Multivariate Machine Learning Methods for Fusing Multimodal Functional Neuroimaging Data. *Proceedings of the IEEE* **103**, 1507-1530, doi:10.1109/JPROC.2015.2425807 (2015).

8 Warbrick, T., Arrubla, J., Boers, F., Neuner, I. & Shah, N. J. J. J. Attention to Detail: Why Considering Task Demands Is Essential for Single-Trial Analysis of BOLD Correlates of the Visual P1 and N1. *Journal of cognitive neuroscience* **26**, 1--14, doi:10.1162/jocn (2013).

9 Baumeister, S. *et al.* Sequential inhibitory control processes assessed through simultaneous EEG-fMRI. *NeuroImage*, doi:10.1016/j.neuroimage.2014.01.023 (2014).

10 Novitskiy, N., Ramautar, J. R. & Vanderperren, K. a. The BOLD correlates of the visual P1 and N1 in single-trial analysis of simultaneous EEG-fMRI recordings during a spatial detection task. *NeuroImage* **54**, 824--835, doi:10.1016/j.neuroimage.2010.09.041 (2010).

11 Nguyen, V. T. & Cunnington, R. The superior temporal sulcus and the N170 during face processing: Single trial analysis of concurrent EEG-fMRI. *NeuroImage*, doi:10.1016/j.neuroimage.2013.10.047 (2013).

12 De Martino, F. *et al.* Multimodal imaging: an evaluation of univariate and multivariate methods for simultaneous EEG/fMRI. *Magnetic resonance imaging* **28**, 1104-1112, doi:10.1016/j.mri.2009.12.026 (2010).

13 Mayhew, S. D., Ostwald, D., Porcaro, C. & Bagshaw, A. P. Spontaneous EEG alpha oscillation interacts with positive and negative BOLD responses in the visual-auditory cortices and default-mode network. *NeuroImage* **76**, 362-372, doi:10.1016/j.neuroimage.2013.02.070 (2013).

14 Jann, K. *et al.* BOLD correlates of EEG alpha phase-locking and the fMRI default mode network. *NeuroImage* **45**, 903-916, doi:10.1016/j.neuroimage.2009.01.001 (2009).

15 Jaspers-Fayer, F., Ertl, M., Leicht, G., Leupelt, A. & Mulert, C. Single-trial EEG-fMRI coupling of the emotional auditory early posterior negativity. *NeuroImage* **62**, 1807-1814, doi:10.1016/j.neuroimage.2012.05.018 (2012).

16 Omata, K., Hanakawa, T., Morimoto, M. & Honda, M. Spontaneous Slow Fluctuation of EEG Alpha Rhythm Reflects Activity in Deep-Brain Structures: A Simultaneous EEG-fMRI Study. *PloS one* **8**, e66869-e66869, doi:10.1371/journal.pone.0066869 (2013).

17 Goldman, R. I. *et al.* Single-trial discrimination for integrating simultaneous EEG and fMRI: identifying cortical areas contributing to trial-to-trial variability in the auditory oddball task. *NeuroImage* **47**, 136-147, doi:10.1016/j.neuroimage.2009.03.062 (2009).

18 Walz, J. M. *et al.* Simultaneous EEG-fMRI Reveals Temporal Evolution of Coupling between Supramodal Cortical Attention Networks and the Brainstem. *The Journal of neuroscience : the official journal of the Society for Neuroscience* **33**, 19212-19222, doi:10.1523/jneurosci.2649-13.2013 (2013).

19 Fouragnan, E., Retzler, C., Mullinger, K. & Philiastides, M. G. Two spatiotemporally distinct value systems shape reward-based learning in the human brain. *Nature communications* **6**, 8107, doi:10.1038/ncomms9107 (2015).

20 Naselaris, T., Kay, K. N., Nishimoto, S. & Gallant, J. L. Encoding and decoding in fMRI. *NeuroImage* **56**, 400-410, doi:10.1016/j.neuroimage.2010.07.073 (2011).

21 Hansen, K. A., Kay, K. N. & Gallant, J. L. Topographic organization in and near human visual area V4. *Journal of Neuroscience* **27**, 11896--11911, doi:10.1523/JNEUROSCI.2991-07.2007 (2007).

22 Kay, K. N., Naselaris, T., Prenger, R. J. & Gallant, J. L. Identifying natural images from human brain activity. *Nature* **452**, 352--355, doi:10.1038/nature06713 (2008).

23 Nishimoto, S. *et al.* Reconstructing visual experiences from brain activity evoked by natural movies. *Current Biology* **21**, 1641--1646, doi:10.1016/j.cub.2011.08.031 (2011).

24 Silbert, L. J., Honey, C. J., Simony, E., Poeppel, D. & Hasson, U. Coupled neural systems underlie the production and comprehension of naturalistic narrative speech. *Proceedings of the National Academy of Sciences* **111**, E4687--E4696, doi:10.1073/pnas.1323812111 (2014).

25 Horikawa, T., Tamaki, M., Miyawaki, Y. & Kamitani, Y. Neural decoding of visual imagery during sleep. *Science (New York, N.Y.)* **340**, 639-642, doi:10.1126/science.1234330 (2013).

26 Philiastides, M. G., Ratcliff, R. & Sajda, P. Neural representation of task difficulty and decision making during perceptual categorization: a timing diagram. *The Journal of neuroscience : the official journal of the Society for Neuroscience* **26**, 8965-8975, doi:10.1523/JNEUROSCI.1655-06.2006 (2006).

27 Banko, E. M., Gal, V., Kortvelyes, J., Kovacs, G. & Vidnyanszky, Z. Dissociating the effect of noise on sensory processing and overall decision difficulty. *The Journal of neuroscience : the official journal of the Society for Neuroscience* **31**, 2663-2674, doi:10.1523/JNEUROSCI.2725-10.2011 (2011).

28 Erickson, D. T. & Kayser, A. S. The neural representation of sensorimotor transformations in a human perceptual decision making network. *NeuroImage* **79C**, 340-350, doi:10.1016/j.neuroimage.2013.04.085 (2013).

29 Heekeren, H. R., Marrett, S., Bandettini, P. a. & Ungerleider, L. G. A general mechanism for perceptual decision-making in the human brain. *Nature* **431**, 859-862, doi:10.1038/nature02966 (2004).

30 Philiastides, M. G. & Sajda, P. EEG-informed fMRI reveals spatiotemporal characteristics of perceptual decision making. *The Journal of neuroscience : the official journal of the Society for Neuroscience* **27**, 13082-13091, doi:10.1523/JNEUROSCI.3540-07.2007 (2007).

31 Parra, L. C., Spence, C. D., Gerson, A. D. & Sajda, P. Recipes for the linear analysis of EEG. *NeuroImage* **28**, 326-341, doi:10.1016/j.neuroimage.2005.05.032 (2005).

32 Sajda, P., Philiastides, M. G. & Parra, L. C. Single-trial analysis of neuroimaging data: inferring neural networks underlying perceptual decision-making in the human brain. *IEEE Rev Biomed Eng* **2**, 97-109, doi:10.1109/RBME.2009.2034535 (2009).

33 Muraskin, J., Sherwin, J. & Sajda, P. Knowing when not to swing: EEG evidence that enhanced perception-action coupling underlies baseball batter expertise. *NeuroImage* **123**, 1-10, doi:10.1016/j.neuroimage.2015.08.028 (2015).

34 Sherwin, J., Muraskin, J. & Sajda, P. You Can't Think and Hit at the Same Time: Neural Correlates of Baseball Pitch Classification. *Frontiers in neuroscience* **6**, 177, doi:10.3389/fnins.2012.00177 (2012).

35 Philiastides, M. G. & Sajda, P. Temporal characterization of the neural correlates of perceptual decision making in the human brain. *Cereb Cortex* **16**, 509-518, doi:10.1093/cercor/bhi130 (2006).

36 Cukur, T., Nishimoto, S., Huth, A. G. & Gallant, J. L. Attention during natural vision warps semantic representation across the human brain. *Nature neuroscience* **16**, 763-770, doi:10.1038/nn.3381 (2013).

37 Naselaris, T., Kay, K. N., Nishimoto, S. & Gallant, J. L. Vol. 56 400-410 (2011).

38 Stansbury, D., Naselaris, T. & Gallant, J. Natural Scene Statistics Account for the Representation of Scene Categories in Human Visual Cortex. *Neuron* **79**, 1025--1034, doi:10.1016/j.neuron.2013.06.034 (2013).

39 Wendel, K. *et al.* EEG/MEG source imaging: methods, challenges, and open issues. *Computational intelligence and neuroscience*, 656092, doi:10.1155/2009/656092 (2009).
40 Friston, K. J., Harrison, L. & Penny, W. Dynamic causal modelling. *NeuroImage* **19**, 1273--1302, doi:10.1016/S1053-8119(03)00202-7 (2003).
41 Deuker, L. *et al.* Memory consolidation by replay of stimulus-specific neural activity. *The Journal of neuroscience : the official journal of the Society for Neuroscience* **33**, 19373-19383, doi:10.1523/JNEUROSCI.0414-13.2013 (2013).
42 Fleming, S. M., Huijgen, J. & Dolan, R. J. Prefrontal contributions to metacognition in perceptual decision making. *The Journal of neuroscience : the official journal of the Society for Neuroscience* **32**, 6117-6125, doi:10.1523/JNEUROSCI.6489-11.2012 (2012).
43 Wiecki, T. V., Sofer, I. & Frank, M. J. HDDM: Hierarchical Bayesian estimation of the Drift-Diffusion Model in Python. *Frontiers in neuroinformatics* **7**, 14, doi:10.3389/fninf.2013.00014 (2013).
44 Ratcliff, R. & McKoon, G. The diffusion decision model: theory and data for two-choice decision tasks. *Neural Comput* **20**, 873--922, doi:10.1162/neco.2008.12-06-420 (2008).
45 Philiastides, M. G., Heekeren, H. R. & Sajda, P. Human Scalp Potentials Reflect a Mixture of Decision-Related Signals during Perceptual Choices. *Journal of Neuroscience* **34**, 16877--16889, doi:10.1523/JNEUROSCI.3012-14.2014 (2014).
46 Kiani, R., Corthell, L. & Shadlen, M. N. Choice certainty is informed by both evidence and decision time. *Neuron* **84**, 1329-1342, doi:10.1016/j.neuron.2014.12.015 (2014).
47 Siegel, M., Buschman, T. J. & Miller, E. K. Cortical information flowduring flexible sensorimotor decisions. *Science* **348**, 1352-1355, doi:10.1126/science.aab0551 (2015).
48 Gold, J. I. & Shadlen, M. N. The neural basis of decision making. *Annual review of neuroscience* **30**, 535-574, doi:10.1146/annurev.neuro.29.051605.113038 (2007).
49 Warbrick, T. *et al.* Single-trial P3 amplitude and latency informed event-related fMRI models yield different BOLD response patterns to a target detection task. *NeuroImage* **47**, 1532-1544, doi:10.1016/j.neuroimage.2009.05.082 (2009).
50 Walz, J. M. *et al.* Simultaneous EEG-fMRI reveals a temporal cascade of task-related and default-mode activations during a simple target detection task. *NeuroImage* **102 Pt 1**, 229-239, doi:10.1016/j.neuroimage.2013.08.014 (2014).
51 Yeung, N. & Summerfield, C. Metacognition in human decision-making: confidence and error monitoring. *Philosophical transactions of the Royal Society of London. Series B, Biological sciences* **367**, 1310-1321, doi:10.1098/rstb.2011.0416 (2012).
52 Steinhauser, M. & Yeung, N. Decision processes in human performance monitoring. *The Journal of neuroscience : the official journal of the Society for Neuroscience* **30**, 15643-15653, doi:10.1523/JNEUROSCI.1899-10.2010 (2010).
53 Gherman, S. & Philiastides, M. G. Neural representations of confidence emerge from the process of decision formation during perceptual choices. *NeuroImage* **106**, 134-143, doi:10.1016/j.neuroimage.2014.11.036 (2015).

54 Heereman, J., Walter, H. & Heekeren, H. R. A task-independent neural representation of subjective certainty in visual perception. *Front Hum Neurosci* **9**, 551, doi:10.3389/fnhum.2015.00551 (2015).

55 Botvinick, M. M., Braver, T. S., Barch, D. M., Carter, C. S. & Cohen, J. D. Conflict monitoring and cognitive control. *Psychological review* **108**, 624-652 (2001).

56 Dakin, S. C., Hess, R. F., Ledgeway, T. & Achtman, R. L. What causes non-monotonic tuning of fMRI response to noisy images? *Current biology : CB* **12**, R476-477; author reply R478 (2002).

57 Sajda, P., Goldman, R. I., Dyrholm, M. & Brown, T. R. *Signal Processing and Machine Learning for Single-trial Analysis of Simultaneously Acquired EEG and fMRI*. (Elsevier Inc., 2010).

58 Sajda, P., Goldman, R. I., Philiastides, M. G., Gerson, A. D. & Brown, T. R. A System for Single-trial Analysis of Simultaneously Acquired EEG and fMRI. *2007 3rd International IEEE/EMBS Conference on Neural Engineering*, doi:10.1109/CNE.2007.369667 (2007).

59 Zhang, Y., Brady, M. & Smith, S. Segmentation of brain MR images through a hidden Markov random field model and the expectation-maximization algorithm. *IEEE transactions on medical imaging* **20**, 45--57, doi:10.1109/42.906424 (2001).

60 Greve, D. N. & Fischl, B. Accurate and robust brain image alignment using boundary-based registration. *NeuroImage* **48**, 63--72, doi:10.1016/j.neuroimage.2009.06.060 (2009).

61 Conroy, B. R., Walz, J. M. & Sajda, P. Fast bootstrapping and permutation testing for assessing reproducibility and interpretability of multivariate FMRI decoding models. *PloS one* **8**, e79271, doi:10.1371/journal.pone.0079271 (2013).

62 Sherwin, J. & Sajda, P. Musical experts recruit action-related neural structures in harmonic anomaly detection: evidence for embodied cognition in expertise. *Brain and Cognition* **83**, 190-202, doi:10.1016/j.bandc.2013.07.002 (2013).

63 Strang, G. Introduction to Linear Algebra. *Mathematics of Computation* **18**, 510, doi:10.2307/2003783 (2003).

64 Nichols, T. & Hayasaka, S. Controlling the familywise error rate in functional neuroimaging: a comparative review. *Statistical methods in medical research* **12**, 419--446, doi:10.1191/0962280203sm341ra (2003).

65 Mumford, J. A., Turner, B. O., Ashby, F. G. & Poldrack, R. A. Deconvolving BOLD activation in event-related designs for multivoxel pattern classification analyses. *NeuroImage* **59**, 2636-2643, doi:10.1016/j.neuroimage.2011.08.076 (2012).

66 Darlington, R. B. & Hayes, A. F. Combining independent p values: extensions of the Stouffer and binomial methods. *Psychological methods* **5**, 496-515, doi:10.1037/1082-989X.5.4.496 (2000).

67 Benjamini, Y. & Hochberg, Y. Controlling the False Discovery Rate: A Practical and Powerful Approach to Multiple Testing. *Journal of the Royal Statistical Society. Series B (Methodological)* **57**, 289 -- 300, doi:10.2307/2346101 (1995).

68 Smith, S. M. & Nichols, T. E. Threshold-free cluster enhancement: addressing problems of smoothing, threshold dependence and localisation in cluster inference. *NeuroImage* **44**, 83-98, doi:10.1016/j.neuroimage.2008.03.061 (2009).

69 Stephan, K. E. *et al.* Ten simple rules for dynamic causal modeling. *NeuroImage* **49**, 3099--3109, doi:10.1016/j.neuroimage.2009.11.015 (2010).

70 Penny, W. D. *et al.* Comparing families of dynamic causal models. *PLoS Computational Biology* **6**, doi:10.1371/journal.pcbi.1000709 (2010).

71 Bates, D., Mächler, M., Bolker, B. & Walker, S. Fitting Linear Mixed-Effects Models Using lme4. *2015* **67**, 48, doi:10.18637/jss.v067.i01 (2015).

840
841 ***Figure Captions***

842 Figure 1. **Paradigm and traditional EEG and fMRI results**

843 **A,** 3-AFC task where stimulus evidence for each category is modulated by varying the
844 phase coherence in the images. **B,** Example of face images with high stimulus evidence
845 (high coherence: 50%) and low stimulus evidence (low coherence: 35%). **C,** Behavioral
846 performance shows significant differences, as a function of stimulus evidence, in
847 accuracy ($p< 10^{-12}$, paired t-test) and **D,** response time ($p< 10^{-8}$, paired t-test) across the
848 group. **E,** Grand average stimulus-locked event related potentials (ERPs) for electrode Pz
849 show that differences in stimulus evidence span the time from stimulus to response. **F**,
850 fMRI analysis showing cortical areas correlated with high (red) vs. low (blue) stimulus
851 evidence across the entire trial ($Z> 2.57$ with $p< 0.01$ Family-Wise Error cluster
852 corrected).

853 Figure 2. **Temporally precise trial-to-trial EEG variability tags brain regions during**
854 **decision-making**

855 **A**, Illustration of how trial-to-trial variability of neural activity in spatially distinct
856 cortical areas can be used to tag brain regions. In this hypothetical example Region 1 is
857 involved in sensory encoding while Region 2 integrates sensory evidence to form a
858 decision (in NHP literature, Region 1 might represent MT, while Region 2 LIP). Neural
859 activity across the trial is shown for two stimulus types, one with high sensory evidence
860 for the choice (red curves) and one with low sensory evidence (blue curves). Also
861 shown are two temporal windows (τ_1 and τ_2) that represent different times during the
862 trial. **B**, Linear classifiers are trained to separate trials based on the two levels of stimulus
863 evidence at specific temporal windows. Shown are classifiers (parameterized by weight

vectors w_1 and w_2) for two temporal windows (τ_1 and τ_2) with respect to two EEG sensors (for simplicity only two dimensions of the full N=43 sensor space are shown. Though the component hyperplane is optimal for the full 43 dimensions, when projected to a line in two dimensions for illustration, it may appear that the separation is sub-optimal). This yields an EEG discriminant component for each temporal window. Variability along these components serves as a unique feature vector for temporally tagging the BOLD data—e.g. variability along an EEG component trained with data from τ_1 tags BOLD voxels with time τ_1 while variability along an EEG component trained with data from τ_2 tags them with τ_2.

Figure 3. **Encoding models based on stimulus derived features versus EEG variability**

A, A traditional encoding model used in fMRI analysis extracts a set of features from the stimulus that are potentially representative of low level structure and high level semantics (green box). Weights are learned to model how these stimulus features are encoded in the fMRI BOLD signal. The resulting encoding model is used to make predictions based on how well different voxels predict the features from novel stimuli. For example, one can create maps of the brain that are labeled based on the stimulus features that each voxel represents. **B**, The same encoding model concept applied to EEG variability (EEG encoding model). Instead of features being estimated from the stimulus, they are derived from EEG component trial-to-trial variability (as in Fig 2a) with each temporal window representing a different feature (green box). Weights are learned so as to model how the EEG variability at a given time window is encoded in the fMRI BOLD. As in the

traditional encoding model, predictions on novel stimuli can be done to test the model and results can be used to construct a map —in this case a map of the brain that shows the timing of the EEG component variability that each voxels represents.

Figure 4. **EEG discrimination and encoding model results**

A, Group average area under the receiver operating curve (AUC) for the sliding window logistic regression EEG discrimination analysis, comparing high versus low stimulus evidence trials; standard error across subjects is shown with shading. **B**, A single subject's discriminating y-value distributions for high (red) and low stimulus evidence (blue) trials for two EEG time points (225ms and 600ms). **C**, Significant fMRI voxels resulting from the group level analysis for the encoding model ($p< 0.01$ TFCE-False Discovery Rate (FDR) corrected). Activity is seen encompassing early visual processing regions, attention networks, and the task positive network. **D**, A random subset of 100 (50 for each stimulus evidence condition) from 700 total trials of the actual (circle) and predicted (diamond) BOLD responses from the encoding model, for an example subject at a single voxel (MNI X/Y/Zmm: -27/-54/-15, $r=0.206$, $p<10^{-6}$). High and low stimulus evidence trials are shown separately for clarity. **E**, The averaged correlation of the predicted y-values with the true y-values across the trial duration. Blue shading represents the standard error across subjects. Grey shading indicates significant time windows ($p< 0.05$ FDR-corrected).

Figure 5. **Group-level encoding model weights results show neural activation cascade**

909 Subset of thresholded (p< 0.05 FDR-Corrected, k=10) group level statistical parametric
910 maps created by stTFCE randomization procedure on the encoding model weight
911 matrices show the progression of spatial activity across the trial. Activation can be seen
912 early in the trial in the occipital regions while progressing more anteriorly later in the trial
913 to executive control areas. Activations in red indicate areas where high stimulus evidence
914 trials had larger activations than low stimulus evidence trials, and blue the inverse.
915
916 Figure 6. **Spatial-temporal event-related activations show coordinated reactivations.**
917 **A,** Union across time windows of significant voxels for high (red) and low (blue)
918 stimulus evidence activations. Voxels with activations for both high and low conditions
919 (at different time windows) are displayed in green. Also shown are the encoding model
920 weights for specific voxels, including fusiform gyrus (FG-R):36/-51/-18, (FG-L):-42/-
921 42/-18, superior lateral occipital cortex (sLOC):24/-63/36, superior parietal lobule
922 (SPL):27/-51/54, anterior cingulate cortex (ACC):-6/24/30, intraparietal sulcus (IPS):-
923 30/-60/39, middle frontal gyrus (MFG):-45/27/30, middle temporal gyrus (MT):-57/-
924 60/0. Asterisks indicate significant windows. **B**, Sequence of significant weights showing
925 a "replay" of the network after the onset of ACC activation (shaded ellipse). "Replay" is
926 faster than the initial stimulus driven sequence and strongest for low evidence trials.
927
928 Figure 7. **Trial-to-trial reactivation correlates with decision confidence.**
929 Trial-to-trial reactivation amplitude ($Y_{j,i}^{R}$ – see Methods) of "replay" correlates with
930 confidence proxy for both high (**A)** and low (**B**) stimulus evidence conditions. Error bars
931 represent standard errors across subjects. (**C**), Stimulus-locked replay activation clusters

and feature importance. **(inset)** Regions of interest used in computing the reactivation values for computing confidence proxy correlations. These regions were taken from significant group activations from 600-800ms post stimulus. Regions were then clustered (> 48 voxels) and a secondary analysis for feature importance was performed. Here, we removed each cluster before computing trial-to-trial reactivations and compared the slope of reactivation x confidence proxy when all clusters were present. Panel **C** shows the ranking of feature importance for each cluster (more negative % change = more importance). Negative changes in slopes show that by removing that cluster the slope of the correlation between reactivation and confidence decreases, indicating the importance of that cluster. Increases in slope indicate that the correlation is higher with that region removed.

Figures:

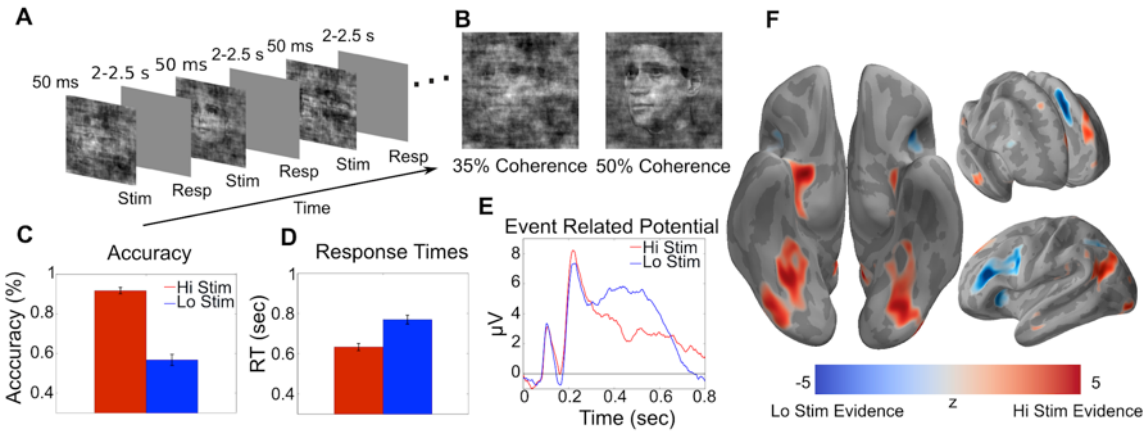

Figure 1.

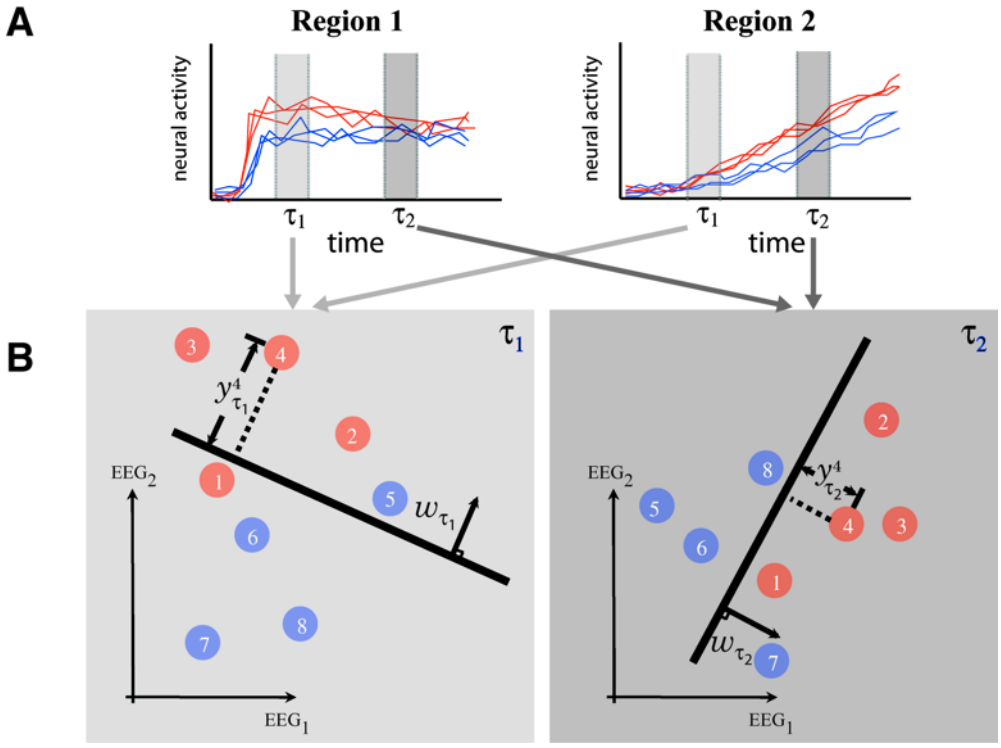
A
Region 1
Region 2
neural activity
neural activity
τ_1
τ_2
time
τ_1
τ_2
time
B
τ_1
τ_2
$y^4_{\tau_1}$
w_{τ_1}
$y^4_{\tau_2}$
w_{τ_2}
EEG$_2$
EEG$_1$
EEG$_2$
EEG$_1$

Figure 2.

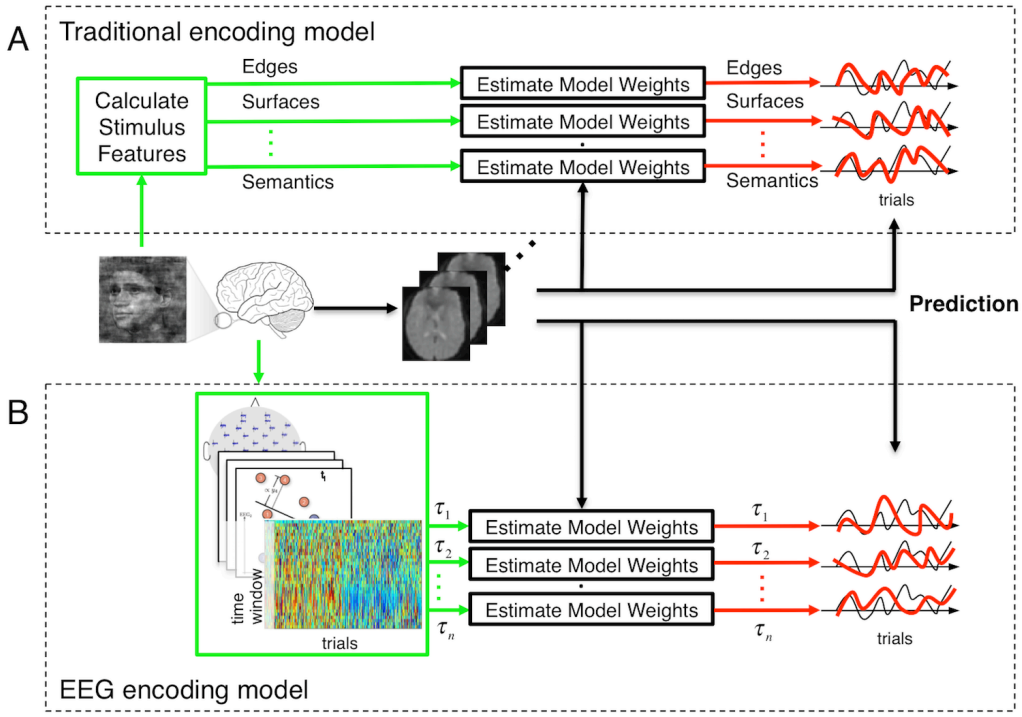
A
Traditional encoding model
Calculate Stimulus Features
Edges
Surfaces
Semantics
Estimate Model Weights
Estimate Model Weights
Estimate Model Weights
Edges
Surfaces
Semantics
trials
Prediction
B
time window
trials
τ_1
τ_2
τ_n
Estimate Model Weights
Estimate Model Weights
Estimate Model Weights
τ_1
τ_2
τ_n
trials
EEG encoding model

Figure 3.

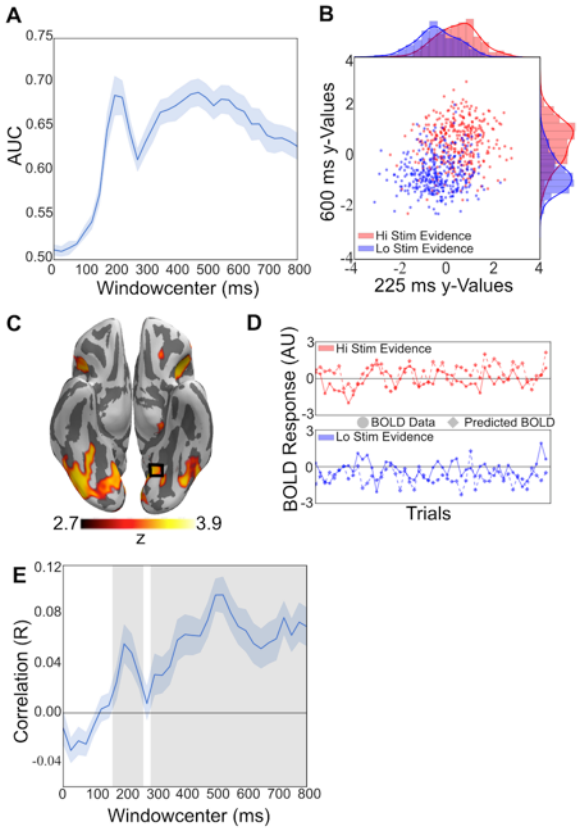
A
AUC
Windowcenter (ms)
B
600 ms y-Values
225 ms y-Values
Hi Stim Evidence
Lo Stim Evidence
C
2.7
3.9
z
D
BOLD Response (AU)
Hi Stim Evidence
BOLD Data
Predicted BOLD
Lo Stim Evidence
Trials
E
Correlation (R)
Windowcenter (ms)

Figure 4.

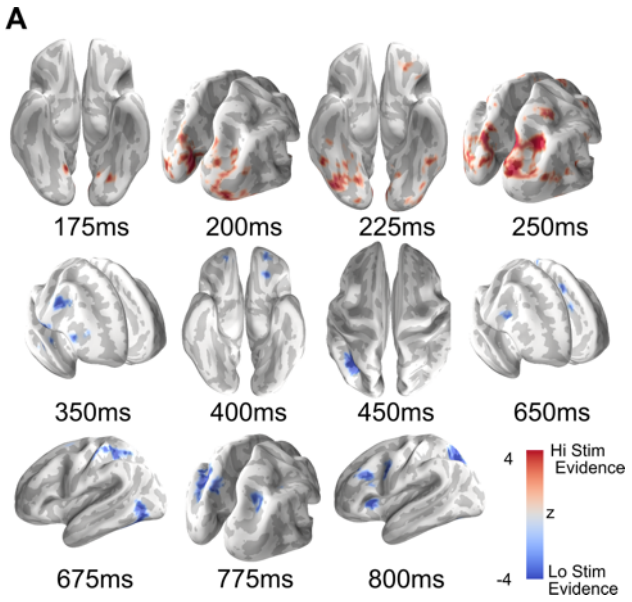
A
175ms
200ms
225ms
250ms
350ms
400ms
450ms
650ms
675ms
775ms
800ms
4
Hi Stim Evidence
z
-4
Lo Stim Evidence

Figure 5.

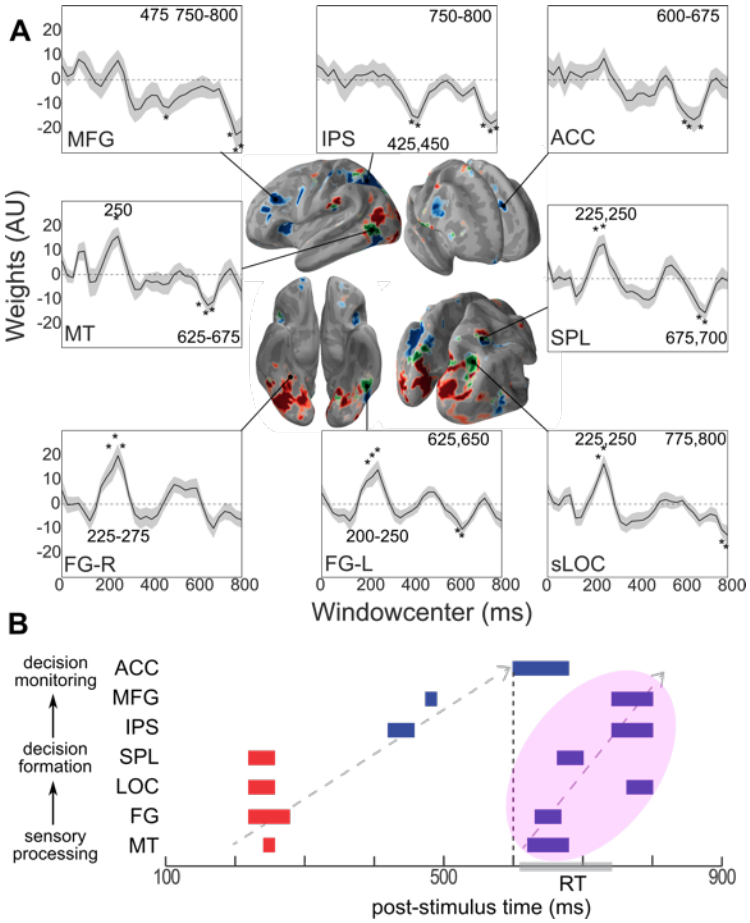
A
475 750-800
MFG
750-800
IPS
425,450
600-675
ACC
250
MT
625-675
225,250
SPL
675,700
Weights (AU)
625,650
225,250
775,800
225-275
FG-R
200-250
FG-L
sLOC
Windowcenter (ms)
B
decision monitoring
decision formation
sensory processing
ACC
MFG
IPS
SPL
LOC
FG
MT
100
500
RT
900
post-stimulus time (ms)

Figure 6.

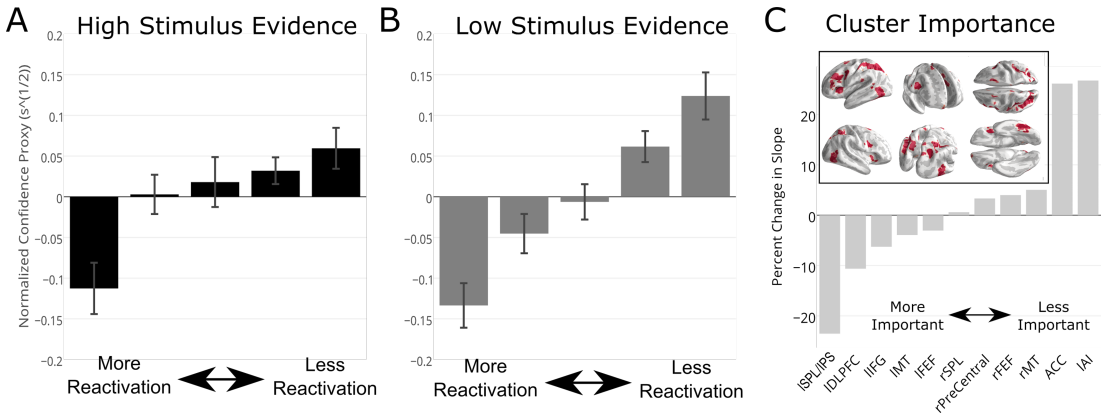
A
High Stimulus Evidence
Normalized Confidence Proxy (s^(1/2))
0.2
0.15
0.1
0.05
0
−0.05
−0.1
−0.15
−0.2
More Reactivation
Less Reactivation
B
Low Stimulus Evidence
0.2
0.15
0.1
0.05
0
−0.05
−0.1
−0.15
−0.2
More Reactivation
Less Reactivation
C
Cluster Importance
Percent Change in Slope
20
10
0
−10
−20
More Important
Less Important
lSPL/IPS
lDLPFC
lIFG
lMT
lFEF
rSPL
rPreCentral
rFEF
rMT
ACC
lAI

Figure 7.